https://doi.org/10.5194/egusphere-2025-1256
Preprint. Discussion started: 28 March 2025

Subauroral Crosstalk in POES/Metop TED Channels

Jan Maik Wissing[1], Olesya Yakovchuk[2], Stefan Bender[3], and Christina Arras[4,5]

[1]German Aerospace Center (DLR), Institute for Solar-Terrestrial Physics, Neustrelitz, Germany
[2]Institute of Physics, University of Rostock, Rostock, Germany
[3]Instituto de Astrofísica de Andalucía, Granada, Spain
[4]GFZ Helmholtz-Centre for Geosciences, Potsdam, Germany
[5]Berlin University of Technology, Berlin, Germany

Correspondence: Jan Maik Wissing (jan.wissing@dlr.de)

Abstract. Particle measurements from the Polar Operational Environmental Satellites (POES) and their successor, the Meteorological Operational (Metop) satellite program, are widely used for various scientific applications. While most studies focus on the Medium Energy Proton and Electron Detector (MEPED), the low-energy (eV and keV) counterpart, the Total Energy Detector (TED), has received comparatively less attention. However, the recent rise in the altitudes considered in ionization and climate models has increased interest in low-energy particle measurements as inputs for atmospheric ionization models.

This study analyzes TED particle data (along with selected MEPED channels) from 2001 to 2018 and demonstrates that, in particular, the TED 0° proton channels—and, to a lesser extent, other TED channels as well as the MEPED proton channels P1, P2, and P3—are contaminated by energetic electrons at $L < 6$ (with the exception of TED electron band 4). In some cases, the contaminated fluxes exceed typical auroral flux levels. The affected regions were cross-validated using auroral UV emissions and occurrences of GNSS derived *S4 index* to rule out the possibility that the observed fluxes correspond to real particle precipitation.

Additionally, we established a Kp- and channel-dependent latitude boundary that may serve as a simple cut-off criterion for the contaminated regions. Furthermore, we propose a more general flux correction approach based on background count measurements.

1 Introduction

Accurate spaceborne particle measurements are essential for various scientific fields, particularly for modeling the atmospheric impact of precipitating particles. These impacts include direct ionization and the production of nitrogen oxides (NO_x) (Rusch et al., 1981) and hydroxyl (OH) (Solomon et al., 1981, 1983), which can lead to catalytic processes such as ozone depletion (Crutzen et al., 1975; Heath et al., 1977; McPeters and Jackman, 1985; Funke et al., 2011). In the case of TED protons, these effects are primarily confined to NO_x production in the lower thermosphere, between 130 and 150 km. Due to its link to ozone chemistry, particle precipitation may also influence the radiation budget and, consequently, atmospheric dynamics.

However, particle measurements are often affected by various sources of bias, including crosstalk from different energies or particle species, out-of-view contamination, electric charging, and detector degradation. For the POES/Metop MEPED

https://doi.org/10.5194/egusphere-2025-1256
Preprint. Discussion started: 28 March 2025

instrument, these issues have been extensively discussed and quantified. For instance, MEPED electron channels are known to suffer from proton contamination (Evans and Greer, 2004b), which has been addressed using correction methods that subtract the spectral contribution of interfering protons (Lam et al., 2010; Asikainen and Mursula, 2013; Peck et al., 2015; Nesse Tyssøy et al., 2016). Monte Carlo simulations have also been employed to model the theoretical MEPED detector response to various particle species and energies (Yando et al., 2011). These simulations indicate that MEPED proton detectors are affected by energetic electron crosstalk, with the strongest impact on channel P1, decreasing in higher-energy channels. Additionally, proton detector degradation, which becomes significant after 2–3 years in orbit, has been quantified using orbit intersections of different satellites (Asikainen et al., 2012). MEPED detector degradation has also been quantified by (Asikainen and Mursula, 2011; Ødegaard et al., 2016; Sandanger et al., 2015).

In contrast, studies on the data quality of the POES/Metop TED instrument remain scarce. The instrument description (Green, 2013) acknowledges energetic protons from the South Atlantic Anomaly (SAA) and energetic electrons from the radiation belts as primary sources of TED background counts. A correction for TED energy flux based on background count measurements is proposed in (Green, 2013), yet significant contamination from energetic electrons appears to persist. For example, Søraas et al. (2018, Figures 4 and 5) observed a daily modulation in TED observations of sub-20 keV electrons between 50° and 62° ILAT during the 17 March 2013 geomagnetic storm, which they attributed to the penetration of relativistic electrons. However, no dedicated crosstalk analysis or correction has been conducted for the various TED energy bands. Given the growing demand for accurate low-energy particle measurements to support high-altitude atmospheric precipitation studies (e.g., Wissing and Kallenrode, 2009), this study aims to address that gap.

High-energy particle populations known to induce crosstalk are typically found within the radiation belts. For over 50 years, Earth's radiation belts have been understood to consist of two distinct zones—an inner and an outer belt—separated by the so-called slot region (van Allen, 1959, 1983). The inner radiation belt primarily contains electrons in the 100 keV range and energetic protons exceeding 100 MeV, which are trapped by relatively strong magnetic fields. This belt typically spans $L = 1.2$ to $L = 2.5$ and remains relatively stable during quiet geomagnetic conditions (e.g., Selesnick et al., 2014). However, strong geomagnetic storms can significantly alter the inner belt proton population (e.g., Selesnick et al., 2014), and in regions such as the SAA, the inner boundary may extend as low as 200 km above Earth's surface. The outer radiation belt, in contrast, consists of highly dynamic electron populations (0.1–10 MeV) with its intensity peaking between $L = 3.5$ and $L = 5.5$ and modulated by geomagnetic activity (e.g., Baker et al., 2013). In 2013, observations from the Van Allen Probes revealed a long-lived relativistic electron storage ring-a third radiation belt-that persisted for four weeks (Baker et al., 2013).

Crosstalk contamination within the radiation belts has been documented for the POES/Metop MEPED instrument. For instance, Andersson et al. (2014) reported elevated MEPED electron count rates in the SAA that did not correspond to mesospheric OH enhancements, suggesting proton crosstalk as the likely cause. Similarly, Evans et al. (2008) identified anomalous increases in the POES E>16 MeV proton channel at subauroral latitudes near the SAA, which they attributed to crosstalk from E>3 MeV electrons.

During our analysis of TED data from POES and Metop satellites for the period 2001–2018, we identified very high fluxes-primarily in the proton bands-at subauroral latitudes. To investigate this phenomenon, we compared TED data with high-energy

https://doi.org/10.5194/egusphere-2025-1256
Preprint. Discussion started: 28 March 2025

electron fluxes, TED background counts, and atmospheric measurements. Our findings indicate strong contamination, most likely from highly relativistic electrons, affecting the low-energy TED proton bands.

The objectives of this study are twofold: a) To establish a simple latitudinal cut-off to exclude the crosstalk-dominated region, thereby enabling the safe application of TED data. b) To develop a crosstalk correction method that can be applied to average TED fluxes, provided background counts are known, and that may also serve as an indicator of TED data quality in polar regions.

The structure of this paper is as follows:

Section 2 describes the data sets and processing methods. Section 3 presents the subauroral flux peak observations that motivated this investigation, along with their Kp dependence. Section 4 assesses the reliability of the measurements within the subauroral region. This section consists of five subsections: Subsection 4.1 provides an overview of the SEM-2 instrument's various measurements. Subsection 4.2 explores energetic electron crosstalk as a potential cause of increased count rates at $L = 4$. Subsection 4.3 examines the differing effects of crosstalk on TED species and orientations. Subsection 4.4 evaluates the impact of crosstalk on MEPED detectors. Subsection 4.5 compares observed particle fluxes with independent data sets, demonstrating that TED proton channels do not capture real flux in the subauroral region. Section 5 quantifies the crosstalk effect, with Subsection 5.1 proposing a correction method based on TED background counts. Section 6 summarizes our findings. The Appendix discusses an issue in TED proton Level 1b netCDF (nc) files that, while unrelated to crosstalk, has not been documented elsewhere.

2 Data Sets

This section describes the data sets utilized in this study and outlines the data processing methodology.

2.1 Particle Data

The particle data originates from the Polar Operational Environmental Satellites (POES) and their successor, the Meteorological Operational satellite program (Metop). Both satellite series operate in sun-synchronous orbits at altitudes of approximately 820 km, with a revolution period of about 100 minutes and an inclination of approximately 98.5°. Although these satellites were initially placed in fixed local time orbits (morning-evening or day-night sector), their orbits have gradually drifted over time, enabling near-complete local time coverage.

The particle detectors aboard POES and Metop are identical and integrated within the Space Environment Monitor SEM-2 (Evans and Greer, 2006). The SEM-2 comprises two instruments: the Total Energy Detector (TED) for low-energy particles and the Medium Energy Proton and Electron Detector (MEPED) for medium-energy particles. TED is a cylindrical electrostatic analyzer, while MEPED is a semiconductor detector with passive shielding.

This study focuses on the TED detector, which consists of a set of electrostatic analyzers (ESA). These analyzers utilize curved plates with predefined radii, modulated by different voltages, to allow only particles of specific energies to pass through and reach a channeltron (multiplier) at the end of the curved plates. TED features eight ESAs that differentiate between low

https://doi.org/10.5194/egusphere-2025-1256
Preprint. Discussion started: 28 March 2025

and high energies, along with two inlet openings at 0° and 30°. Additionally, the curvature of the plates is oriented oppositely for protons and electrons. Particle flux measurements are conducted with the ESA plate voltage activated, while background counts are recorded with the voltage deactivated. Although this study primarily focuses on the upward-looking (0°) detector, which is crucial for observing precipitating particles at high latitudes, it also demonstrates that the TED 30° detector is similarly affected. It is important to note that at low latitudes near the magnetic equator, the 0° detector predominantly measures trapped particles.

This study utilizes data from POES satellites 15, 16, 17, 18, and 19, as well as Metop satellites 01 and 02, covering the period from 2001 to 2018. However, data from POES 16 post-2006 has been excluded due to errors in TED measurements. The data has been analyzed both on a 16-second basis and as annual or multi-annual averages.

The differential TED bands used in this study remain uncorrected. While background counts are recorded and the TED data processing algorithm includes a background subtraction step (Green, 2013), this correction applies only to the total energy flux derived from a full energy sweep and not to individual bands. This holds true for both bin-format data prior to 2013 (Evans and Greer, 2004a) and netCDF-format data after 2013 (Green, 2013). The primary distinction between raw data and processed TED bands in the processed-data files is a multiplication by the geometric factor.

The MEPED electron data has been converted into differential flux by subtracting the three nominal integral channels to produce two differential channels (30-100 keV and 100-300 keV). The energy ranges for all particle channels are detailed in Table 1. Additionally, MEPED electron data has been assigned an error value if high-energy protons, which can cause crosstalk, are detected. This filtering was performed on a 2-second basis using the high-energy P7 proton channel from the omni-directional detector as a proxy, with measurements set to an error value when counts exceeded 2 per second. Consequently, MEPED electron data is excluded during strong proton events and within the South Atlantic Anomaly.

2.2 Coordinate System

This study employs the family of Magnetic Apex Coordinates (Van Zandt et al., 1972), which are derived from the International Geomagnetic Reference Field (IGRF). A key advantage of IGRF-based coordinate systems is that they account for the gradual movement of the geomagnetic poles, ensuring consistency in precipitation feature localization over extended time periods. This stability allows for multi-year spatial approximations of precipitation fluxes and facilitates the application of results to future datasets.

For ground-based locations and higher latitudes, Magnetic Apex Coordinates closely resemble the widely used Altitude Adjustment Corrected Geomagnetic (AACGM) coordinates. Specifically, poleward of 50°, the two systems are nearly identical (see Fig. 7 in Laundal and Richmond, 2017).

However, for positions above the ground, Magnetic Apex Coordinates provide a more accurate framework for describing charged particle behavior. These coordinates track the magnetic field lines from their footpoints upward, ensuring that charged particles remain on the same coordinates during their bounce motion. Thus, in Magnetic Apex Coordinates, the altitude of a satellite measurement does not alter the perceived location of a particle.

https://doi.org/10.5194/egusphere-2025-1256
Preprint. Discussion started: 28 March 2025

By default, the reference altitude for magnetic field-line footpoints is set to ground level. However, the Modified Apex Coordinates (Richmond, 1995) enable customization of the reference altitude. In this study, we use a reference altitude of 110 km, approximately where atmospheric interactions begin to dominate over magnetic field influences. Consequently, the coordinate system utilized is termed "Modified Apex 110 km Coordinates," though we may refer to it simply as "APEX" in the text.

2.3 Kp-Binning of Particle Data

The planetary K-index (Kp) (Bartels et al., 1939) quantifies geomagnetic activity using a 3-hourly quasi-logarithmic scale ranging from 0 to 9. It is derived from observations at 13 geomagnetic observatories located between 44° and 60° in both northern and southern geomagnetic latitudes. The Kp index is sensitive to multiple current systems, including the ring current, and thus provides a global measure of magnetospheric activity.

For this study, particle data has been categorized into seven Kp-level groups: 0–0.7, 1–1.7, 2–2.7, 3–3.7, 4–4.7, 5–5.7, and 6–9. This binning approach enables the examination of particle flux variations as a function of geomagnetic activity.

2.4 SSUSI Data Set

We use the electron energy flux data from the Special Sensor Ultraviolet Spectrographic Imager (SSUSI) instruments on board the Defense Meteorological Satellite Program (DMSP) Block-5D3 satellites F17 and F18 (Paxton et al., 1992, 2017, 2018). These satellites orbit at 850 km altitude in polar, sun-synchronous orbits, the equator crossing times of their ascending nodes are 17:34 LT (F17) and 20:00 LT (F18). The SSUSI detectors provide about 3000 km-wide spectrographic images of the auroral zones with a 10 km×10 km pixel size at the nadir point. Of these spectra 5 UV channels are downlinked, including two colours for the LBH (Lyman–Birge–Hopfield) band emissions of N_2. From these two LBH colours the electron energies and energy fluxes are derived based on Strickland et al. (1983), additional discussion can be found in Knight et al. (2018). The electron energy flux data used here are provided within the Auroral-EDR (Environmental Data Record) data set at https://ssusi.jhuapl.edu/data_products (SSUSI, 2020). The data files contain the data point locations in geomagnetic latitude and longitude in AACGM coordinates.

The data have been validated previously by comparing them to EISCAT ground-based observations (Bender et al., 2021). For the comparison here, for each DMSP/SSUSI orbit during 2013, the data points within 60°E ±4° geomagnetic longitude were selected. The electron energy fluxes within these sectors were then averaged in one-degree latitude bins to produce the time series as shown later in Sect. 4.5.2.

It should be said that the SSUSI-derived fluxes are based on the hypothesis that the UV-aurora originates from a pure electron spectrum. There is an on-going discussion how pure proton or mixed auroral spectra would show up in the results of these pure-electron calculations. While model calculations of Knight et al. (2012, their Table 4) and Gelinas and Hecht (2016) agree that this technique should slightly over-estimate the atmospheric peak electron density, Knight (2021) did not see such an overestimation comparing SSUSI-derived atmospheric electron density with ionosonde observations under proton precipitation

https://doi.org/10.5194/egusphere-2025-1256
Preprint. Discussion started: 28 March 2025

conditions. Concerning this paper we may just conclude that –even though the SSUSI algorithms threat all UV lines as effect of electron precipitation– particle precipitation from both, electrons and protons, show up in the SSUSI data set.

2.5 *S4 index*

The *S4 index* is a standard measure used to quantify ionospheric scintillation, referring to rapid fluctuations in the amplitude and phase of radio signals as they pass through irregularities in the ionosphere. It is defined as the ratio of the standard deviation of signal intensity to the average signal intensity (Wu, 2020). For this study, we used *S4 index* values calculated from the signal-to-noise ratio (SNR) of GNSS radio occultation profiles. We analyzed the atmPhs or conPhs data product provided by UCAR for nine different satellite missions (CHAMP, GRACE, Formosat-3/COSMIC-1, PAZ, Spire, TerraSAR-X, TanDEM-X, KompSat-5, Metop-B, Metop-C, and PlanetiQ) measured within the latitude belt between 55°S and 65°S from 2001 to 2024. Further, we concentrated on night-time measurements.

In total, 231,680 radio occultation profiles met our criteria. Using the method described by Arras and Wickert (2018), we calculated the maximum *S4 index* for each profile within the altitude range of 90km to 150km. Profiles that included a sporadic E signature were excluded from further analysis.

3 Observation of High Particle Fluxes in the Subauroral Zone

A distinct local maximum in TED proton flux, separate from both auroral precipitation and the South Atlantic Anomaly (SAA), was previously reported by Yakovchuk and Wissing (2019). This section examines which channels exhibit enhanced subauroral particle flux and how it correlates with geomagnetic activity.

Figure 1 presents the multi-year averaged spatial distribution of TED proton flux for the period 2001–2018, separated by geomagnetic activity levels (left: Kp=0–0.7, right: Kp=4–4.7). A localized increase in flux appears around 60° North and South APEX, with a stronger presence at longitudes that also intersect the SAA (most notably near 60°E APEX in the Southern Hemisphere)

At low Kp levels (Fig. 1, left), the flux distribution of all TED 0° proton channels exhibits a clear separation between the auroral oval and the subauroral peak, as indicated by the red line. However, as geomagnetic activity increases (Fig. 1, right), the separation diminishes, with the auroral flux extending equatorward and merging with the subauroral peak. For Kp levels of 5 and above, the subauroral feature becomes indistinguishable from the auroral precipitation.

The dependence of the subauroral peak on geomagnetic disturbance is further illustrated in Figure 3, which shows cross-sections of *TED 0° proton band 11* at 60°E APEX for different Kp levels. While the subauroral peak consistently appears between 56° and 60° APEX in both hemispheres, increasing geomagnetic activity broadens and intensifies the auroral oval, shifting its equatorial boundary closer to the subauroral feature. As a result, the two regions may merge at moderate Kp levels (e.g., Kp = 4–4.7 in Fig. 1, right, for *TED 0° proton band 14*). However, differences in latitudinal extent and flux intensity suggest that portions of the subauroral peak remain distinguishable at moderate Kp levels. At higher Kp values,

https://doi.org/10.5194/egusphere-2025-1256
Preprint. Discussion started: 28 March 2025

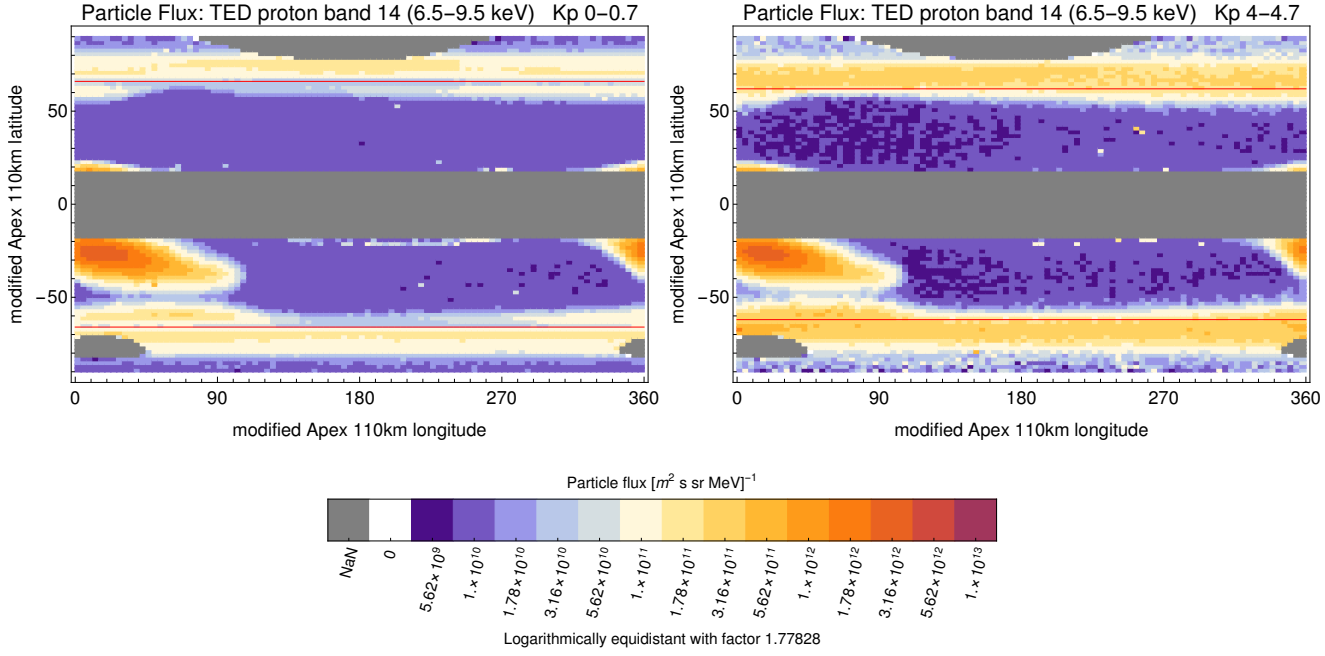

Figure 1. Spatial flux distribution of *TED 0° proton band 14* for selected Kp levels (low Kp: left, medium Kp: right) averaged over the years 2001–2018.

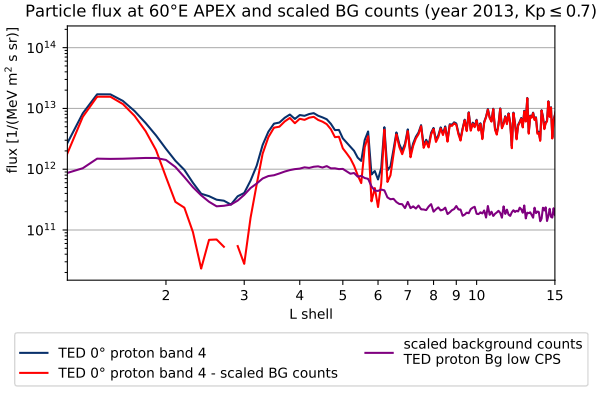

Figure 2. The subauroral peak of the TED channels cannot be adequately corrected based on scaled background counts. Either it creates strong negative fluxes around the peak or the correction does not significantly change the fluxes.

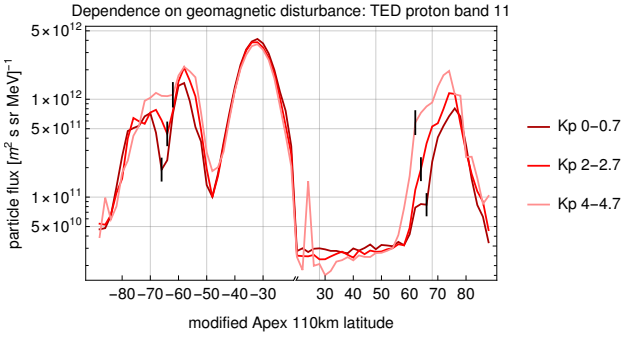

Figure 3. Cross-section at 60°E APEX for *TED 0° proton band 11* during varying levels of geomagnetic disturbance. The vertical lines indicate the minimum between the auroral and subauroral peaks. Note that the latitude axis is stitched together, as modified APEX latitudes at 110 km altitude are constrained to values greater than 18°.

https://doi.org/10.5194/egusphere-2025-1256
Preprint. Discussion started: 28 March 2025

	instrument	channel	energy range	Separation of the contamination area at Kp				
				0–0.7	1–1.7	2–2.7	3–3.7	4–4.7
electrons	TED 0°	band 4	154–224 eV	-	-	-	-	-
		band 8	688–1000 eV	-	-	-	-	-
		band 11	2.115–3.075 keV	-	-	-	-	-
		band 14	6.503–9.457 keV	-	-	-	-	-
	MEPED 0°	e1-e2‡	30–100 keV	62°†‡	-	-	-	-
		e2-e3 ‡	100–300 keV	64°‡	62°‡	-	-	-
protons	TED 0°	band 4	154–224 eV	66°	64°	62°	60°	58°
		band 8	688–1000 eV	66°	64°	64°	62°	62°
		band 11	2.115–3.075 keV	66°	66°	64°	64°	62°
		band 14	6.503–9.457 keV	66°	64°	64°	62°	62°
	MEPED 0°	P1	30–80 keV	-	-	-	-	-
		P2	80–240 keV	62°	-	-	-	-
		P3	240–800 keV	62°	62°†	-	-	-
		P4	0.8–2.5 MeV	-	-	-	-	-
		P5	2.5–6.9 MeV	-	-	-	-	-

Table 1. Channel and Kp combinations that exhibit enhanced subauroral flux, along with the location of the minimum between auroral and subauroral peaks, as identified visually from spatial maps such as Fig. 1. The latitude values apply to both the Northern and Southern Hemispheres. Notes: † *Almost invisible.* ‡ *Subauroral peak is most likely accurate; do not use as a latitudinal cut-off!*

the subauroral peak becomes fully embedded within the auroral precipitation, limiting its identification to periods of low geomagnetic disturbance.

It is worth noting that the northern subauroral peak is generally weaker than its southern counterpart, and 60°E APEX does not intersect its strongest region.

Figure 2 shows the flux of a TED proton band against L-shell. We also added scaled background counts. Scaled background counts are overlaid, with the scaling factor chosen large as possible but still preventing unphysical negative counts at L=2-3 and L=6. The peak at L=4 remains largely unchanged, indicating that no linear background correction can eliminate the subauroral maximum without compromising physical consistency. This suggests that the background-corrected total energy flux may exhibit similar issues, as seen in Søraas et al. (2018, their Figures 4 and 5).

Table 1 summarizes the TED 0° proton channels and Kp conditions under which enhanced subauroral fluxes were detected. The identification criterion required the presence of a local flux maximum exceeding the equatorial boundary of the auroral oval by a factor of at least 1.778 (equivalent to one-quarter of an order of magnitude in logarithmic flux levels) across a significant fraction of longitudes, ruling out statistical fluctuations.

https://doi.org/10.5194/egusphere-2025-1256
Preprint. Discussion started: 28 March 2025

Enhanced subauroral flux is observed across all TED 0° proton channels, whereas no corresponding feature is detected in TED electron data. Some MEPED channels also exhibit weak subauroral peaks, but only at very low Kp levels (Kp$\leq$1.7, and in some cases, only for Kp$\leq$0.7).

To illustrate the potential impact of a misinterpreted subauroral peak, we estimate its contribution to atmospheric ionization. Wissing and Kallenrode (2009, see their Fig. 9, lower panel) reported that at 120 km altitude, auroral proton-induced ionization accounts for approximately 14% of total ionization, with electrons dominating the remaining contribution. If the observed subauroral TED flux is real, it would imply an additional ionization peak at this auroral proton level in the lower thermosphere (130-150 km). This highlights the importance of accurately characterizing the subauroral peak to refine atmospheric chemistry models.

4 Is the Subauroral Peak a Real Flux or an Artifact from Crosstalk?

A critical question regarding the observed subauroral particle fluxes is the reliability of the measurements. As noted in the introduction, high particle fluxes are expected at low L-shells, particularly in the proton and electron radiation belts. Two primary hypotheses can explain the subauroral peak: a) The low-energy proton fluxes could represent a low-energy tail of the radiation belts. b) The observed fluxes result from contaminated detector counts due to high-energy proton or electron crosstalk.

To investigate this, we analyze various particle measurements from the SEM-2 instrument.

4.1 Comparison of Onboard Particle Data

Figure 4 presents the mean particle fluxes recorded by the vertical detectors (0°, left panels) and non-vertical detectors (TED 30°, MEPED 90°, right panels) for the year 2013 under geomagnetically quiet conditions (Kp $\leq$ 0.7). The data are plotted against L-shell along two APEX longitudes: 60°E and 160°E. Below L=6, the upper lines of each color correspond to 60°E APEX, while the lower lines correspond to 160°E APEX. The year 2013 was chosen because NOAA's data format update allowed easy export of TED background sensor counts per second (CPS).

General Trends in the Data: Nearly all channels exhibit two local maxima: a) A peak at L$\leq$2, associated with the South Atlantic Anomaly (SAA). b) A peak in the subauroral region (L = 3–6), with a maximum at L$\approx$4 ($\sim$60° N/S). This pattern is also reflected in the TED background counts (black for lower energy bands 1–8 and gray for higher energy bands 9–16), which increase significantly at these two locations.

The SAA and the Absence of Energetic Protons in the Subauroral Region: The SAA is well known for intense particle crosstalk, particularly affecting MEPED electron channels (Peck et al., 2015). The applied filtering method, which uses the P6 channel, effectively removes heavily contaminated MEPED electron data from the SAA (L$\leq$2).

However, the subauroral data remain unaffected by P6 filtering, which suggests that energetic protons are not responsible for the observed peak. This leaves two possible explanations: a) The TED proton fluxes represent a low-energy tail of the radiation belt. b) The measurements are contaminated by energetic electron crosstalk.

https://doi.org/10.5194/egusphere-2025-1256
Preprint. Discussion started: 28 March 2025

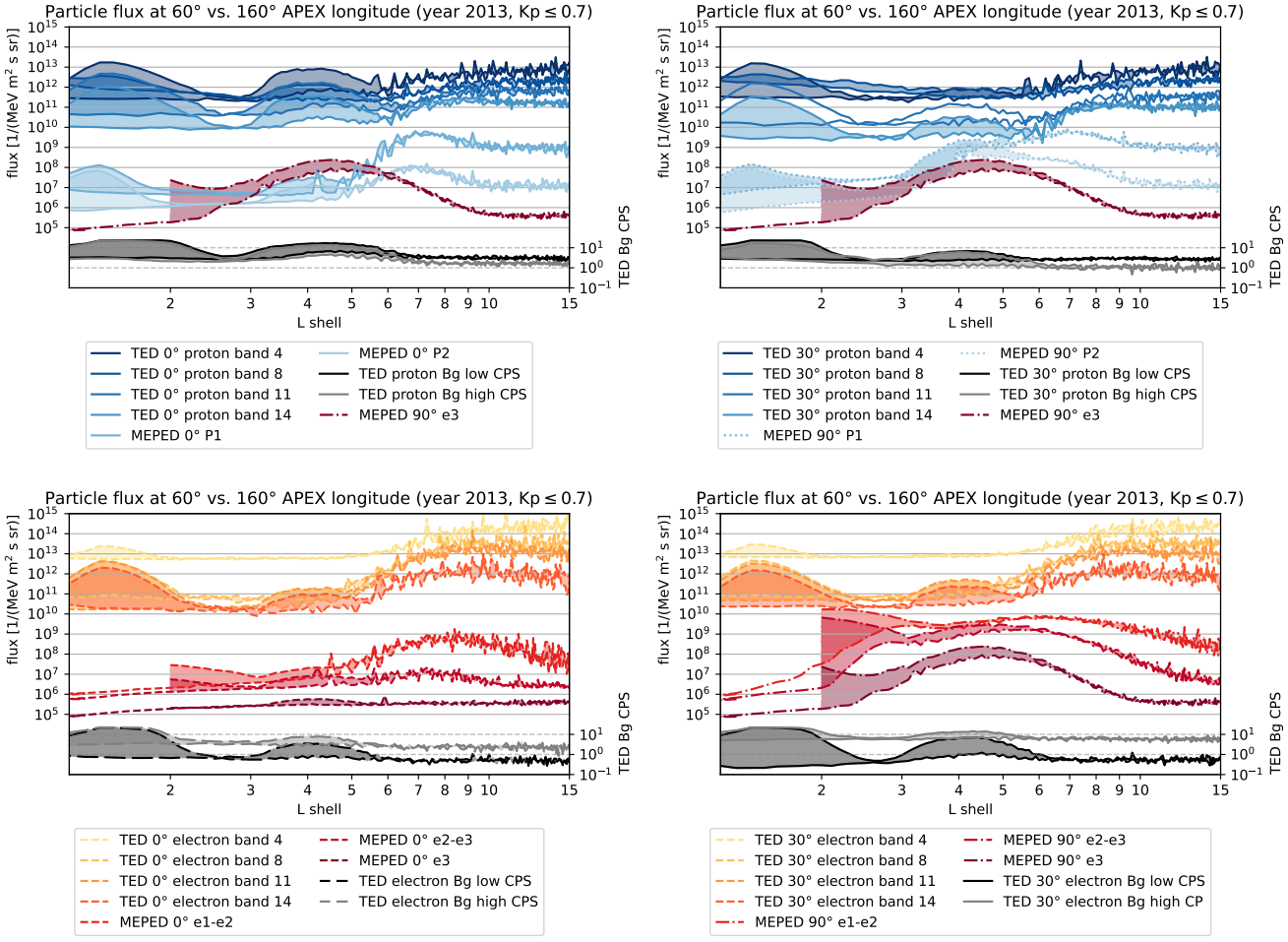

Figure 4. Particle fluxes and background sensor counts for the 0° TED and MEPED detectors (left panels) and the TED 30°/MEPED 90° detectors (right panels). The difference between 60°E and 160°E APEX is highlighted by the shaded area. Below L=6, the higher counts (or fluxes) consistently correspond to 60°E APEX longitude, while the lower values correspond to 160°E APEX. Elevated background counts in the L$\leq$ 2 (SAA) region and in the L$= 3-6$ range (subauroral peak) coincide with intense particle counts in TED proton channels and certain MEPED channels.

Vertical TED Proton Fluxes: To gain further insight, we examine the flux characteristics in the subauroral region, starting with the vertical proton channels (Fig. 4, top left). All vertical TED proton channels exhibit a local maximum at L=4. The flux difference between 60°E APEX (peak) and 160°E APEX (minimum) spans roughly one order of magnitude across all vertical TED channels, albeit from different baseline levels. In contrast, background counts vary by only half an order of magnitude.

Notably, the shape of the background counts differs from the flux peaks. The background counts of vertical TED proton bands form a nearly plateau-like distribution, whereas the measured fluxes show a distinct peak at L=4. If the subauroral peak

https://doi.org/10.5194/egusphere-2025-1256
Preprint. Discussion started: 28 March 2025

were purely due to crosstalk, a simple correction by subtracting background counts (even with a scaling factor) would not effectively remove the contamination.

Vertical MEPED Proton Fluxes: The subauroral peak in *MEPED 0° P1* and P2 is significantly smaller than in the TED protons. Additionally, auroral levels surpass the subauroral peak by two orders of magnitude in *MEPED 0° P1* and one order of magnitude in *MEPED 0° P2*.

Non-Vertical TED Proton Fluxes: A slightly different pattern emerges in the non-vertical TED proton channels (Fig. 4, top right). Here, the background count peak (as well as the flux) is significantly lower than in the vertical channels. Additionally, the longitudinal variation (60°E vs. 160°E APEX) is less pronounced in lower-energy TED channels than in higher-energy ones. Interestingly, the expected subauroral peak in *TED 30° proton band 8* is not clearly observed at L=4, despite noticeable longitudinal differences.

Vertical and Non-Vertical Electron Fluxes: The vertical electron fluxes (Fig. 4, bottom left) exhibit the smallest subauroral peaks among all detectors. In *TED 0° electron band 4*, the peak is absent, likely due to naturally high count rates that mitigate contamination. In *TED 0° electron band 8*, a weak subauroral peak is visible only when comparing 60°E and 160°E APEX. The higher-energy electron channels (*TED 0° electron band 11* and 14) do show a subauroral peak, but it remains one to two orders of magnitude below auroral flux levels.

MEPED electron channels are affected as well. Notably, for *MEPED 0° e3*, the subauroral peak represents the globally highest flux.

For non-vertical electrons (Fig. 4, bottom right), background counts in the subauroral region are higher than for vertical electrons. *TED 30° electron band 4* remains unaffected, whereas the other TED electron channels show similar 60°E–160°E differences, with subauroral peak fluxes surpassing the vertical case.

The MEPED electron channels display a unique behavior. Missing high fluxes in the polar region, only a single maximum (excluding the SAA) is visible. As energy increases, this peak shifts toward lower L-shells and (probably) aligns with the subauroral peak. The highest-energy channel, *MEPED 90° e3*, peaks between L=4 and L=5, indicating the presence of trapped fluxes due to the 90° detector orientation.

4.2 What might be the reason for increased background counts?

Energetic protons have already been excluded due to missing count rates in P6, but according to Li et al. (2001); Baker et al. (2013); Baker et al. (2019), highly relativistic electrons are common at L$=4$ as this region belongs to the electron radiation belts. Additionally, the so-called impenetrable boundary of $>$ 1MeV electrons at about L=2.8 (Baker et al., 2014) fits very well with the background minimum seen in Fig.4.

Energetic electron crosstalk might also explain the Kp dependence, as Turner et al. (2012) point out that the radiation belt electron flux drops by orders of magnitude during geomagnetic storms. A quick radiation belt recovery, which was also noted by Turner et al. (2012), does not contradict this statement as it takes place during lower Kp-values. The same is shown in Ross et al. (2021). Their Fig. 14 compares 4.2 MeV radiation belt electron measurements of the Van Allen Probes at different L-shells with Kp. Whenever the Kp rises to higher levels (say above 5), the electron flux decreases by orders of magnitude. This

https://doi.org/10.5194/egusphere-2025-1256
Preprint. Discussion started: 28 March 2025

is most prominently seen at around L≈4. This already is a good indication for radiation belt crosstalk that disappears at higher Kp. Ross et al. (2021) also state that EMIC or hiss waves are responsible for the radiation belt losses, while the contributions depend on particle energy and L-shell.

Comparing the location of the background peak with the 90° MEPED electrons, we can conclude that the crosstalking electrons should have slightly higher energy than *MEPED 90° e3*. Observations from Peck et al. (2015, see their Fig.5) constructing a virtual electron channel e4 (300 keV–2.5 MeV, same energy range as e3 but higher energy center of 800 keV, based on the MEPED P6 proton channel) show a flux maximum at L= 4, similar to Ross et al. (2021) for 4.2 MeV electrons.

4.3 Why do not all TED channels show the same background counts?

The background counts, as well as the channels' difference between 60°E and 160°E APEX, are highest for vertical TED protons and non-vertical TED electrons, while non-vertical TED protons and vertical TED electrons show less impact.

The shielding of the TED instrument is unfortunately completely undocumented. Using very rough estimations on the volume, mass, and material, we end up with an eventual tungsten shielding of probably less than 0.8 mm, which would allow penetration of electrons >2MeV according to the ESTAR database[1] from NIST. However, this is very vague. According to private communication with Juan Rodriguez (NOAA), it might be better to assess crosstalk candidates by coincidence.

This, however, does not explain any differences between the detectors. In fact, we found a TED detector image that we could combine with information on the size of the single detector openings, which allowed us to determine the layout of the TED detector stack, being from side to side: 0° protons, 30° protons, 0° electrons, 30° electrons. Given that both inner detectors show fewer background counts, we can conclude that this is an effect of better (lateral) shielding.

4.4 Possible crosstalk in the MEPED detectors

The MEPED instrument also shows possible crosstalk characteristics. While the channels *MEPED 0° P2*, P3, *MEPED 0° e1-e2*, and *MEPED 0° e2-e3* have been identified already in Tab. 1, Fig. 4 supports potential crosstalk in *MEPED 0° P1* and the non-vertical *MEPED 90° P1* and P2. As the subauroral region has a strong energetic electron component, it is hard to tell from Fig. 4 which MEPED electron channels might suffer from crosstalk.

For the MEPED detector, Yando et al. (2011) performed Geant4 simulations that revealed a high sensitivity for energetic (radiation belt) electron incidents in the proton channels *MEPED 0° P1*, P2, and P3 (and their 90° equivalents). The MEPED electron channels *MEPED 0° e1*, e2, and e3 (as well as their 90° equivalents) are sensitive to high-energy electrons as they are integral channels without a clear upper energy threshold (compare Yando et al., 2011, for modeled sensitivity). The construction of differential channels by subtracting the higher electron channel was chosen to eliminate an unknown upper energy threshold. According to Yando et al. (2011), the geometric factor differs between the two low energetic channels e1 and e2 and the higher e3 channel for electron incidents above approximately 800 keV. For 3 MeV electrons, the geometric factor of e1 and e2 is four times higher than for e3. Therefore, subtracting neighboring channels should eliminate energetic electron crosstalk from *MEPED 0° e1-e2*, but it may not completely eliminate high-energy electron crosstalk from the *MEPED 0° e2-e3*.

[1] https://physics.nist.gov/PhysRefData/Star/Text/ESTAR.html

https://doi.org/10.5194/egusphere-2025-1256
Preprint. Discussion started: 28 March 2025

The shielding of the MEPED detector housing should eliminate out-of-view electron crosstalk only up to about 6 MeV (Evans and Greer, 2004b). Consequently, this may be a source of crosstalk inside the radiation belts. On the other hand, Selesnick et al. (2020) showed that especially during periods of low pitch angle diffusion (equivalent to low Kp), most of the detector counts at L=4 in the 0° detector result from trapped or quasi-trapped (out-of-nominal field-of-view) electrons. In this sense, a determination of the precipitating flux based on the 0° detector would lead to a significant overestimation. Therefore, the crosstalk might not be restricted to relativistic electrons but also includes out-of-view contamination.

We should also note that the MEPED electron channels might be affected by crosstalk from low-energy protons (see Yando et al., 2011) as the MEPED electron channels have not been corrected for this.

To conclude this subsection, we can say that the abundance of high-energy electrons is most likely responsible for the TED background counts and suggests that crosstalk in the TED proton channels (and to some extent in the other channels) is occurring. However, due to the absence of a correction algorithm, this does not provide a direct measure of the actual abundance of low-energy particles. In other words, it remains unclear whether the crosstalk is strong enough to fully account for the observed peaks in the low-energy channels.

4.5 Comparison to Different Data Sets

The most relevant datasets for comparison are those from satellites with similar orbits. However, these datasets often suffer from the same issue – particle measurements in the radiation belts are problematic and frequently omitted. For instance, data from the METEOR-3M satellite program (accessible at https://ftp.sinp.msu.ru/meteor-3m/msgi/L1/ and http://smdc.sinp.msu.ru/) are subject to such limitations.

To circumvent this issue, we adopted a different approach. If the peak observed in the low-energy 0° detectors is real, it should manifest as particle precipitation in the atmosphere at the footpoints of the corresponding magnetic field lines (which coincide in APEX coordinates). To assess the atmospheric impact, we applied two independent methods. First, we examined the *S4 index*: a peak in TED proton flux at TED energies should result in an ionization peak at approximately 150 km altitude, which should be reflected in the *S4 index*. Second, particle interactions in the upper atmosphere should produce UV radiation, which can be detected using auroral imagers such as SSUSI.

4.5.1 Comparison to *S4 index*

Figure 5 compares the *S4 index* (top panel), which serves as an indicator for ionization layer formation, with the particle flux from an affected TED channel, *TED 0° proton band 11* (middle and bottom panels).

The S4 profiles in the first panel have been restricted to night-time[2]. The night-time *S4 index* is elevated between 80°–190°E geographic with a main peak at 100-120°E.

The second panel illustrates the long-term particle flux for *TED 0° proton band 11* without any Kp filtering. A wave-like structure (orange) originates from the auroral oval in geographic coordinates, reaching latitudes closest to the equator at 90–

[2]Including day-time *S4 index* would produce a second maximum at maximum at 270°E geographic –not associated with particle precipitation but being an artifact of the subsolar TEC maximum that expands into the observed domain only in the area of the SAA.

https://doi.org/10.5194/egusphere-2025-1256
Preprint. Discussion started: 28 March 2025

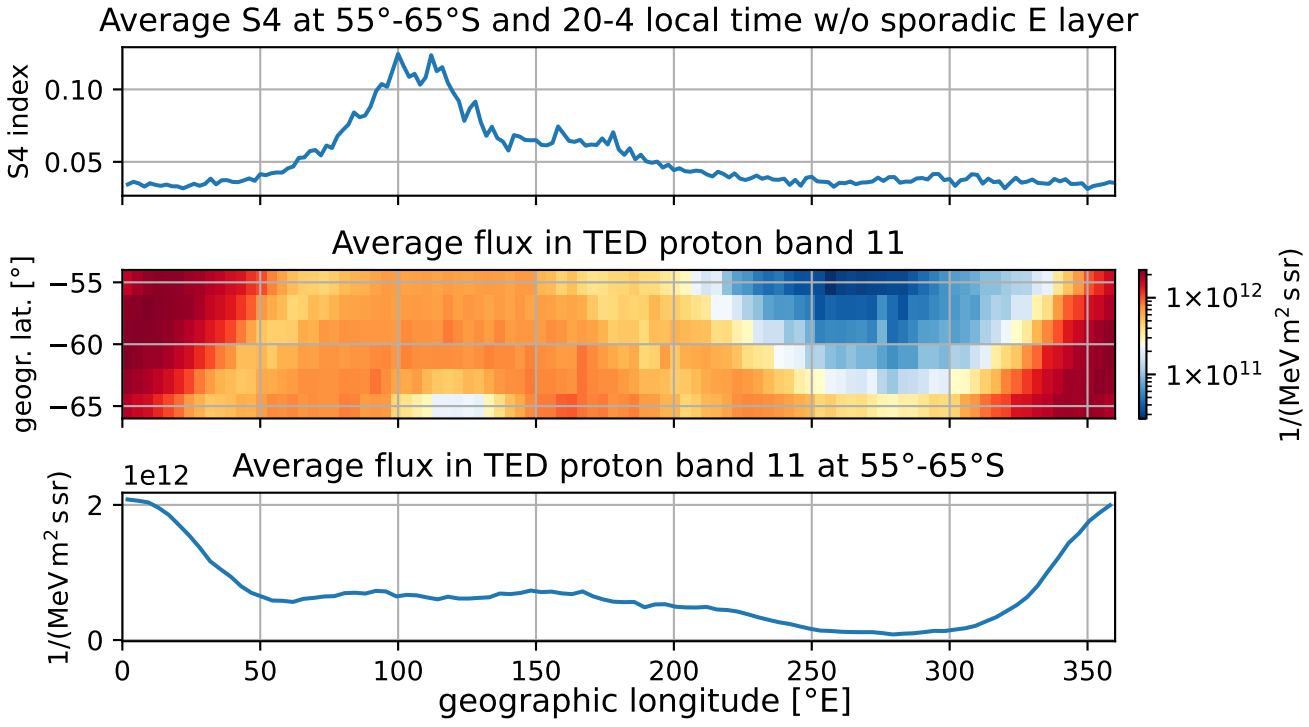

Figure 5. The top panel shows the GNSS-derived *S4 index* at 55–65°S, averaged over all available night-time (20–4 local time) profiles from 2001 to 2024 that do not exhibit a sporadic E-layer. The *S4 index* serves as an indicator of disturbances in the ionosphere. The middle panel presents the average particle flux in *TED 0° proton band 11* for the same latitudinal band, covering the years 2001–2018. The bottom panel condenses the middle panel's data into a latitudinal mean, allowing for direct comparison with the *S4 index*.

150°E geographic. The highest flux values (above 10^{12} $/(MeV\,s\,sr\,m^2)$, in red) occur between 320° and 50°E geographic, corresponding to subauroral latitudes in APEX coordinates. The lowest flux values (blue) appear between 250° and 300°E geographic, aligning with a region equatorward of the subauroral peak.

The bottom panel condenses the 2D information from the middle panel into a latitudinal mean, allowing direct comparison with the top panel. The peak in the *S4 index* at 110°E geographic arises from particle precipitation in the auroral region. Notably, bottom and top panels exhibit a double-peak structure (at 110°E and 150°E geographic), which is a result of the limited energy range of the observed channel. Lower-energy particles would create an auroral pattern that extends further poleward, leading to a single peak.

Crucially, in the region between 320° and 50°E geographic, where the TED channel registers a flux maximum, the *S4 index* does not indicate a corresponding ionization increase. Since particle precipitation at a specific energy should produce a distinct ionization signature at a predictable altitude, the low *S4 index* suggests that the observed TED proton flux in this region is a detector artifact.

https://doi.org/10.5194/egusphere-2025-1256
Preprint. Discussion started: 28 March 2025

4.5.2 Comparison to SSUSI

Figure 6 (top panel) presents the total precipitating proton energy flux derived from all 0° TED proton channels and *MEPED 0° P1*, covering an energy range of 154 eV to 80 keV. Two regions exhibit increased flux: one centered around 70°S APEX latitude, indicative of auroral precipitation, and another at 60°S APEX latitude, corresponding to the subauroral peak. Periods of Kp$\geq$ 5 are marked by blue lines in the upper part of the graph and also shown in the bottom panel. The subauroral peaks tend to follow periods of elevated Kp, and in some cases, the subauroral proton energy flux exceeds that of the auroral region. Two instances of strong subauroral peaks are highlighted for comparison.

The second panel displays the electron energy flux (154 eV to 100 keV) from the TED 0° electron channels and *MEPED 0° e1-e2*. Unlike the proton flux, the subauroral electron contribution is significantly smaller, while the auroral electron flux is more pronounced. Additionally, auroral electron flux is strongly dependent on geomagnetic activity, intensifying and shifting equatorward during high Kp conditions. The proton flux exhibits similar behavior, albeit at lower intensities.

The third panel combines proton and electron energy fluxes. The subauroral contribution is comparable to auroral levels, underscoring the need to determine whether the subauroral flux is real or an artifact.

Panels 4 and 5 present UV-derived energy fluxes from auroral emissions measured by DMSP-17 and DMSP-18, respectively. Both datasets exhibit a strong Kp dependence, with increased energy flux during geomagnetic disturbances and auroral emissions extending to approximately 60°S APEX latitude. This aligns with the electron flux observations in the second panel. However, the marked subauroral peak does not appear in the UV data, even though the combined energy flux matches levels recognized as auroral emissions. This suggests that the subauroral proton energy flux is overestimated.

Given the similarities in detector design, it is likely that the TED electron channels experience subauroral crosstalk contamination. However, since the subauroral electron flux is lower, it may not be detectable in SSUSI data.

In summary, Figures 5 and 6 independently demonstrate–through the absence of ionization effects and auroral emissions–that the subauroral peak does not correspond to real precipitating low-energy particles. The only times when precipitation effects are recorded in this region coincide with geomagnetic storms, during which the auroral oval expands into this latitude range (see Fig. 6, second panel).

Note that Figure 5 is not very sensitive to high Kp particle precipitation. First, the temporal contribution is small and second all shown latitudes would be similarly affected, resulting in a mostly longitude-independent S4 offset.

It is worth noting that Kavanagh et al. (2018) observed particle precipitation events at L<4 (slot region) using MEPED electron channels, detecting electrons exceeding 640 keV (potentially above 1 MeV) and corroborating these findings with riometer measurements. These so-called slot region filling events persist long after the storms that generate them and exhibit low Kp dependence. However, our observation methods, which focus on the upper atmosphere, do not capture deep atmospheric ionization (occurring in the lower mesosphere to stratopause, 50–55 km altitude). This suggests that while an energetic electron population is often present at low Kp, contributing to deep atmospheric ionization and crosstalk, the majority of TED proton channel fluxes during these periods are likely artifacts.

https://doi.org/10.5194/egusphere-2025-1256
Preprint. Discussion started: 28 March 2025

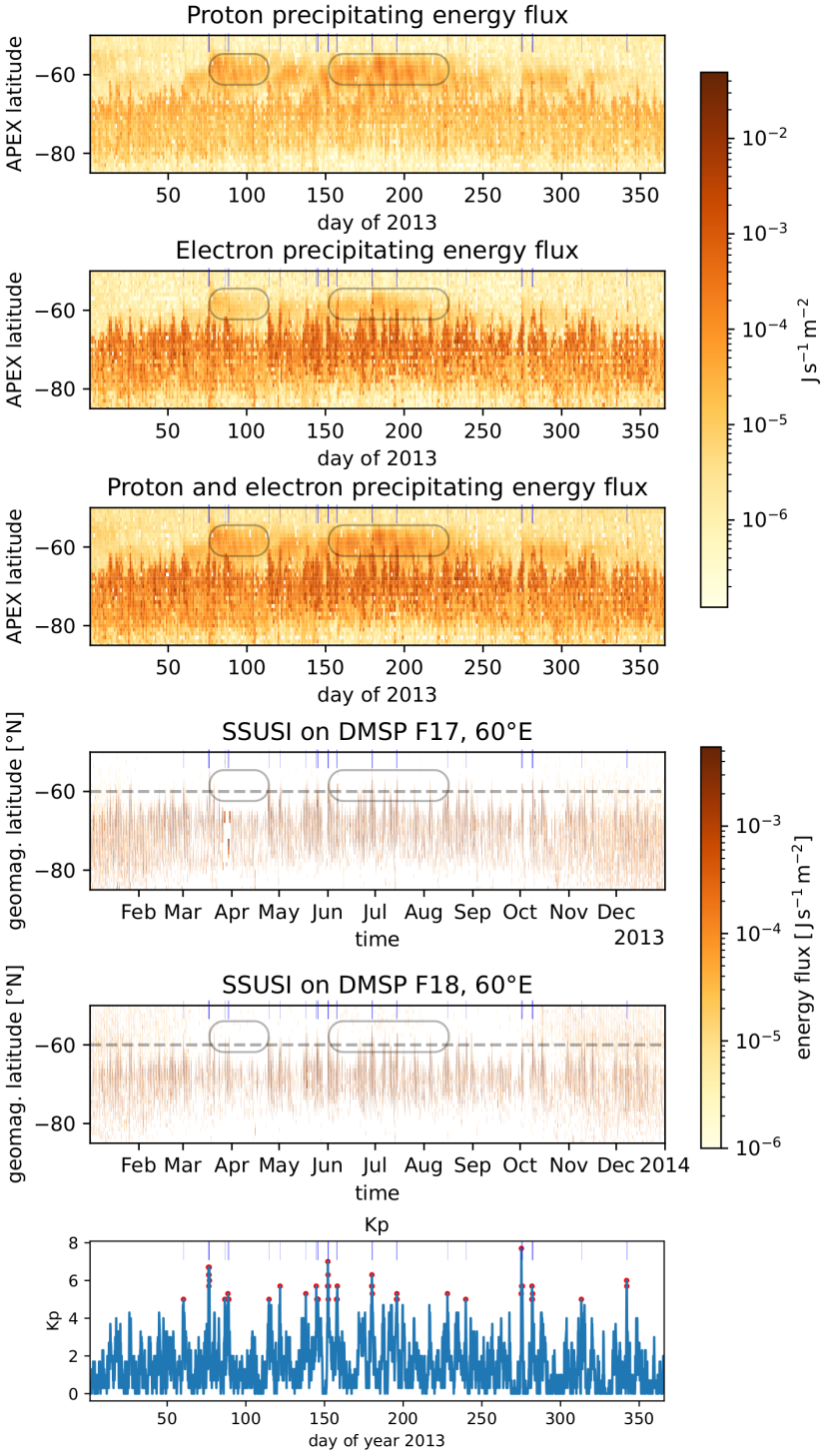

Figure 6. Temporal evolution of electron energy flux, proton energy flux, and their combined flux, compared to auroral UV radiation from SSUSI observed by two satellites, and the geomagnetic activity represented by Kp for the year 2013.

https://doi.org/10.5194/egusphere-2025-1256
Preprint. Discussion started: 28 March 2025

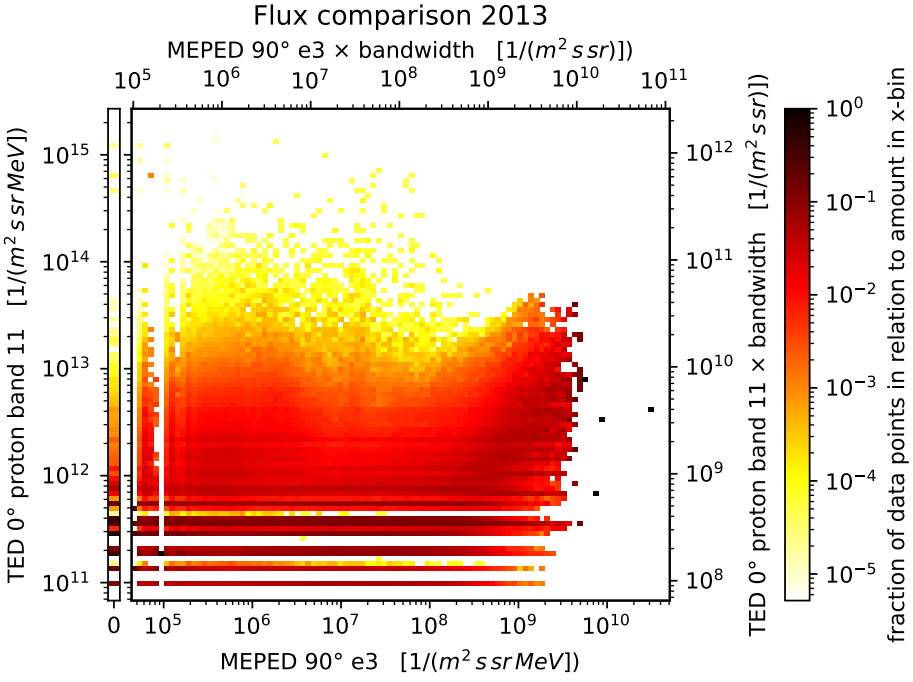

Figure 7. Correlation of *TED 0° proton band 11* and *MEPED 90° e3*.

It is important to note that disproving the existence of a subauroral low-energy proton peak during low Kp does not invalidate the possibility of subauroral proton precipitation in general. Kim et al. (2021) linked low-energy subauroral proton precipitation to EMIC wave activity. However, their study focused on substorm periods without significant fluxes of electrons exceeding 100 keV.

5 Estimation of Crosstalk

Figure 7 illustrates the correlation between *TED 0° proton band 11* and *MEPED 90° e3* throughout 2013. The largest subfigure reveals two distinct particle populations. At low *MEPED 90° e3* flux levels (up to approximately $10^8/(m^2\,s\,sr\,MeV)$), the *TED 0° proton band 11* flux distribution remains largely independent of the electron flux. However, beyond this threshold, the peak fraction of the TED proton flux distribution (dark red area) increases with rising energetic electron flux. Notably, most data points in this second population originate from the subauroral region.

As demonstrated in Section 4, particularly in Subsection 4.5, the elevated TED fluxes in subauroral regions are not real. This strong correlation is a clear indication of crosstalk.

One might argue that the large difference in flux levels between these channels should prevent significant crosstalk; however, this is not the case. The secondary axis in Figure 7 presents integral fluxes across the full bandwidth of each channel. Within

https://doi.org/10.5194/egusphere-2025-1256
Preprint. Discussion started: 28 March 2025

the correlated population, the peak fraction of the TED proton flux distribution follows a roughly one-to-one relationship with *MEPED 90° e3*, albeit with considerable spread. Additionally, *MEPED 90° e3* does not even peak at the same L-shell location, suggesting that a higher-energy electron channel–such as the virtual electron channel proposed by Peck et al. (2015)–might yield an even stronger correlation.

Another factor to consider is that both particle channels can record zero flux, indicating that the detectors' integration time may be insufficient to capture a meaningful flux level. Zeros in *MEPED 90° e3* are binned separately (see the left graph in Fig. 7), while *TED 0° proton band 11* registers zero flux at 16-second resolution in approximately 60% of cases, with this fraction decreasing above $3 \times 10^7/(m^2\, s\, sr\, MeV)$.

In conclusion, *TED 0° proton band 11*–and likely other TED channels–should be treated with caution when *MEPED 90° e3* flux levels exceed $10^8/(m^2\, s\, sr\, MeV)$. Due to the significant spread in the data, a simple subtraction of *MEPED 90° e3* scaled by its bandwidth would yield unreliable results and is therefore not recommended.

5.1 Correction Based on TED Background Counts

A natural approach to correcting TED bands involves subtracting background counts, as applied by Green (2013) for total energy flux. However, Figure 4 (e.g., top left) and Figure 2 highlight two key challenges: (1) a proper conversion of background counts to physical flux is required, and (2) a non-linear response must be accounted for. The background peaks observed in the South Atlantic Anomaly (SAA) and the subauroral region flatten at high values, a behavior not seen in uncorrected TED flux or the crosstalking *MEPED 0° e3* peak. Consequently, applying a simple linear scaling to match SSUSI observations at subauroral latitudes would introduce unphysical negative fluxes at L=2.5–3.

Three potential sources of non-linearity come to mind. First, saturation effects may arise due to the longer integration time of the background detector (3.2 s) compared to 0.2 s for individual band measurements. However, the highest recorded background counts remain below 30–far from the allowed maximum of 1,999,848 stated in Green (2013). Second, non-linearity could stem from data compression during satellite transmission (see Table 14 in Green, 2013). Yet, since we observe non-integer values, we trust that these represent decompressed counts (see Table 15 in Green, 2013, and notes in the netCDF files). Third, orbital motion during measurement could contribute: background counts are averaged over 16 instrument cycles (32 s total), during which the satellite travels about 270 km (or 1° latitude). This spatial averaging naturally smooths background peaks compared to individual band measurements.

The underlying assumption for an empirical crosstalk correction is that a given background count level corresponds to a predictable level of crosstalk in the particle bands. Since multiple flux measurements exist for each background count level, the lowest observed flux should best approximate the crosstalk component. We thus use the dataset from Figure 4 (without longitudinal restrictions) to estimate the lower flux envelope for each background count value.

Figure 8 shows the background estimation by correlating background counts with individual particle bands. Three main groups emerge, illustrated using *TED 0° proton band 11* (top panel, third column). The first group (blue, as in Fig. 4), centered around (10^0, 3×10^{11}), represents mostly uncontaminated flux. The second group (gray) forms a narrow band extending to

https://doi.org/10.5194/egusphere-2025-1256
Preprint. Discussion started: 28 March 2025

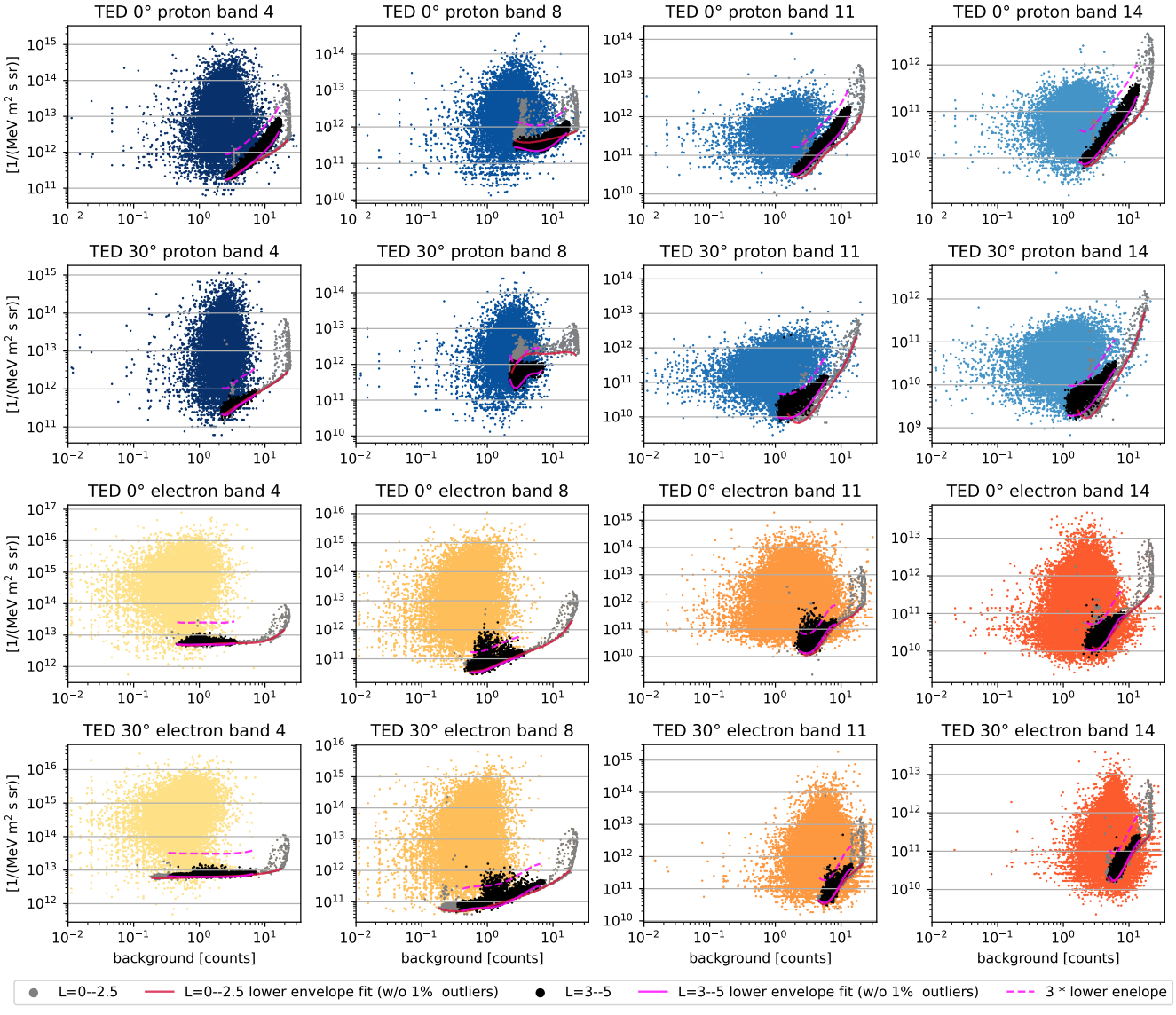

Figure 8. Correlation of TED channels and their individual background channel.

the highest background counts ($> 10^1$) and corresponds to the SAA, where background channels reach a plateau, possibly indicating saturation. The third group (black), located between the others, corresponds to the subauroral region.

Notably, crosstalk effects appear more pronounced in the lateral detectors (first and last row), as indicated by higher background counts and steeper black point distributions.

Differences in crosstalk behavior between proton and electron detectors are also evident: while electron channels exhibit a smooth transition between the gray and black regions, proton bands–especially the higher-energy ones–respond differently in

https://doi.org/10.5194/egusphere-2025-1256
Preprint. Discussion started: 28 March 2025

TED band	L=0–2.5 a	b	c	d	e	L=3–5 a	b	c	d	e
0° proton 4	2.051	-6.1816	6.4765	-1.642	11.1728	5.7917	-17.9069	20.9118	-9.4183	12.6564
0° proton 8†	1.6316	-6.237	9.0663	-5.546	12.7714	-4.5487	15.5999	-17.437	7.5566	10.3358
0° proton 11	9.9935	-32.2271	37.1218	-16.3454	12.8258	10.1772	-27.8587	27.797	-10.2049	11.7269
0° proton 14	9.0204	-28.6562	32.5691	-14.0791	11.8449	9.0	-25.7265	27.0084	-10.5172	11.2107
30° proton 4	1.0693	-2.9538	2.7254	0.1437	11.0256	48.1375	-119.1584	108.0797	-41.2981	16.9328
30° proton 8†	-8.2545	30.8206	-42.0943	24.9475	6.8832	146.6174	-369.5469	340.4818	-134.3787	30.526
30° proton 11	7.7157	-24.2692	28.7625	-12.43	11.5685	-2.9447	4.7859	0.4545	-0.428	9.9987
30° proton 14	8.9894	-27.4732	31.4856	-13.4727	11.1219	-3.8881	3.9985	1.8121	-0.6905	9.3293
0° electron 4‡	0.7892	-1.1404	0.33	0.1527	12.6766	1.6733	-0.4014	-0.1909	0.026	12.7008
0° electron 8	1.424	-2.4948	1.2059	0.8195	10.657	2.5877	-3.3489	1.0656	0.8774	10.6245
0° electron 11	22.5389	-81.7559	106.4621	-56.3445	20.3689	-43.5699	94.1662	-66.3469	18.0006	8.6601
0° electron 14	13.7024	-50.8715	68.2776	-37.185	17.0847	-30.779	67.4684	-48.2632	13.6192	8.7722
30° electron 4‡	0.103	-0.0274	-0.0285	0.0697	12.7904	0.3535	-0.0563	-0.0375	-0.0097	12.7964
30° electron 8	0.2418	-0.2757	0.2688	0.5322	10.8432	-2.3358	1.9735	0.8169	0.1607	10.8056
30° electron 11	31.9686	-137.3464	217.6068	-148.2536	47.1251	-27.1793	76.5225	-67.7951	18.5156	11.1271
30° electron 14	28.1675	-121.58	193.5498	-132.2969	42.9333	51.2541	-217.6807	342.9869	-234.5949	68.8703

Table 2. Fit parameters of the lower envelope of the crosstalk. † Unusual crosstalk behavior; a latitude-based cut may be preferable. ‡ No significant dependency on background counts in the subauroral region; likely usable without correction. Further details are provided in the text.

the SAA and subauroral region, except for *TED 30° proton band 8*. This suggests a species-dependent crosstalk mechanism. The exact cause remains unclear, but instrument shielding and internal structures likely play a role.

Empirical evidence suggests that the proton channel background derived from the SAA is insufficient for correction in the subauroral region, where typical fluxes at L=4 are an order of magnitude higher. As a result, two distinct background corrections are necessary.

Implementation of Background Correction: To determine the lower envelope, the data were divided into 20 logarithmically spaced background-count bins. Within each bin, data points were sorted by flux, and the logarithmic distance to the following data point is determined. In order to suppress outliers, 1% of the data points are omitted, depenging on this distance. The fit was then applied to the lowest remaining flux value in each bin. The parameters belong to a polynomial that has been fitted to the log_{10} values of background counts b_g and lower envelope channel flux (Φ_{LE}) in form of $\log_{10}(\Phi_{LE}) = a \cdot \log_{10}(b_g)^4 + b \cdot \log_{10}(b_g)^3 + c \cdot \log_{10}(b_g)^2 + d \cdot \log_{10}(b_g) + e$. Fit parameters for the SAA (L=0—2.5) and subauroral region (L=3–5) are presented in Table 2 and depicted in Figure 8.

https://doi.org/10.5194/egusphere-2025-1256
Preprint. Discussion started: 28 March 2025

Corrections appear unnecessary for TED electron band 4, where extremely high flux values overshadow crosstalk effects. This is also seen in the subauroral population which does not show a significant dependency on the background counts (except for the saturation at very high counts).

TED proton band 8 exhibits unexpected behavior, lacking a clear positive correlation and showing stronger proton crosstalk than electron crosstalk. The reason remains unclear, making this channel unsuitable for correction.

For all other channels, the correction method appears valid, provided it is applied within defined boundaries: (1) not below local minima (e.g., TED band 11), (2) not in regions of saturation, and (3) not extrapolated beyond observed data points due to higher-order polynomial fits.

To ensure reliability, corrections are only applied where the flux exceeds five times the lower envelope. For remaining data points, the lower envelope is subtracted.

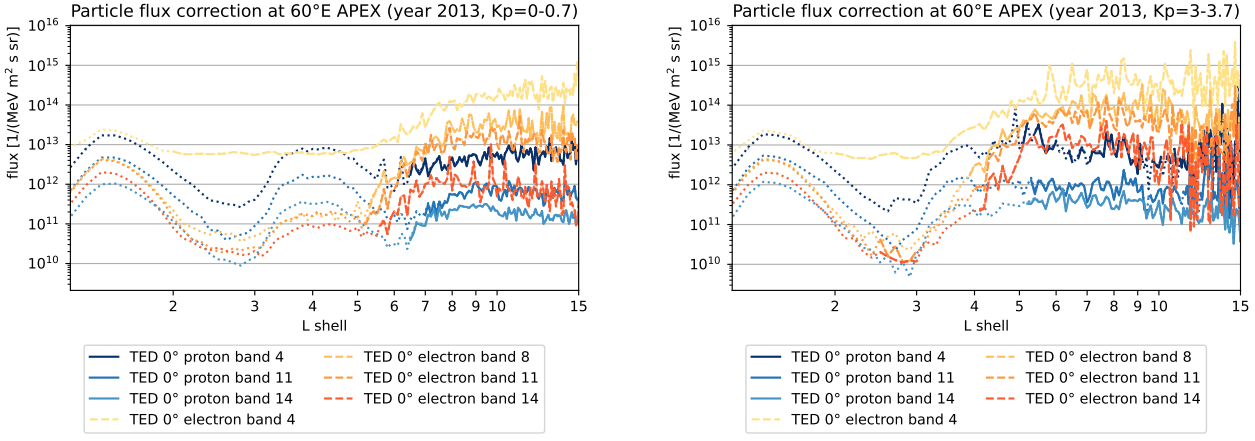

Figure 9. Similar plot as Fig. 4 but with corrected fluxes, two Kp levels and for 60°E APEX only. Note: Dots are uncorrected fluxes.

Figure 9 demonstrates the effect of this correction under different geomagnetic conditions. For Kp=0–0.7, results are comparable to a simple latitudinal cut. However, at Kp=3–3.7, valid flux corrections extend into the subauroral peak, down to L=4 in electron channels. There are also discarded data points even at higher L-shells. We believe that the correction should work properly in this region if the particle species responsible for the elevated background can be identified. Here, we assumed electrons, but using high-energy proton and electron detectors could enable a more accurate selection in open field-line areas.

Note that Figure 9 shows the worst-case scenario, with the strongest background counts occurring at 60°E APEX.

https://doi.org/10.5194/egusphere-2025-1256
Preprint. Discussion started: 28 March 2025

6 Conclusions

In this paper, we investigated the subauroral flux maximum (located at approximately 60°N/S APEX, corresponding to L=4, with a longitudinal focus at 0–100°E APEX, most prominent south of the South Atlantic Anomaly) observed in many TED channels (mainly in the vertical proton channels) and some MEPED channels.

Two independent measurements of atmospheric impact refute the observed subauroral peak of low-energy particle fluxes under low Kp conditions. Only at higher Kp does the broadening auroral oval contribute to low-energy precipitation in subauroral regions. It is important to note that our observational methods are limited to higher altitudes, meaning that precipitating energetic electrons with an ionization peak below 80 km would not be detected.

Increased background counts indicate an instrumental issue, such as crosstalk, even though the absolute background flux counts remain low. The most likely source of increased TED background counts is energetic electrons from the electron radiation belt. The elevated background counts in the TED 0° proton and TED 30° electron channels could be attributed to the detector stack's design.

The vertical channels may be used to derive atmospheric ionization. However, failing to correct for the contaminated subauroral peak–such as in *TED 0° proton band 11* (which registers twice the typical auroral proton flux)–would result in subauroral thermospheric ionization rates reaching approximately 14% of the typical auroral electron ionization rates. This underscores the necessity of a correction method.

Table 1 presents a preliminary latitude-based cut-off approach, limited to channels with a clear crosstalk peak. While this method leads to an underestimation of the precipitating flux (area), crosstalk appears to be the primary subauroral contribution and may be applied without a longitudinal dependence.

Section 5.1 introduces a correction method based on background fluxes. The second method, however, relies on average fluxes, which may present challenges when applied to 16-second resolution data, as TED channels often register zero fluxes in this timeframe. Due to the strong influence of crosstalk, both methods primarily remove the subauroral region for low Kp. However, the second approach may preserve more data in less affected longitudes and dynamically adjust to actual background flux levels.

An overview of the vertical channels, their observed subauroral fluxes relative to auroral fluxes, and corresponding correction considerations is provided below:

***TED 0° proton band 4*, 8, 11, 14:** Strong subauroral crosstalk, often elevated to or above auroral levels. The crosstalk behavior in TED proton band 8 is unexpected and may not be correctable using background counts.

***MEPED 0° P1*:** Subauroral crosstalk is likely but insignificant, being two orders of magnitude below auroral levels.

***MEPED 0° P2*:** Subauroral crosstalk is likely, reaching one order of magnitude below auroral levels.

***TED 0° electron band 4*:** No sign of crosstalk; flux levels are likely too high to be affected.

***TED 0° electron band 8*, 11:** Subauroral crosstalk is likely but not significant, being two orders of magnitude below auroral levels.

***TED 0° electron band 14*:** Subauroral crosstalk is likely, reaching one order of magnitude below auroral levels.

https://doi.org/10.5194/egusphere-2025-1256
Preprint. Discussion started: 28 March 2025

***MEPED 0° e1-e2*:** Should not be affected by energetic electron crosstalk according to Yando et al. (2011), yet it still exhibits a subauroral peak. This is most likely real flux originating from the electron radiation belts.

***MEPED 0° e2-e3* and the integral channel *MEPED 0° e3*:** Given that *MEPED 0° e1-e2* likely represents real flux with a similar subauroral peak–and considering that these channels cover an energy range even closer to the expected electron radiation belt population–this flux is also likely real. This interpretation is supported by riometer observations of particle precipitation during slot-filling events (Kavanagh et al., 2018).

Appendix A: Note on Using TED Proton Data from Level 1b NetCDF Files

When processing TED proton data from the "processed level 1b data" format, special attention is required due to a minor bug affecting all TED proton bands. Ideally, within a 16-second time frame, the data structure should follow the same format as the TED electron bands:

Expected structure: {a, -1, -1, -1, b, -1, -1, -1, c, -1, -1, -1, d, -1, -1, -1}

Here, a,b,c and d represent the flux values in units of $1/(cm^2\,s\,sr\,eV)$, while -1 denotes an error code indicating no measurement in those intervals.

Actual structure in the data: {a+b, -1, -1, -1, -1, -1, -1, -1, c, -1, -1, -1, d, -1, -1, -1}

Although the data appears similar at first glance, it is crucial to note that the first time slot integrates over two time slots instead of one. This discrepancy must be accounted for during data processing. Notably, this issue does not affect the older bin-format data.

Author contributions. Maik conducted most of the analysis and was the primary author of the paper. Olesya contributed to the analysis of TED and MEPED data. Stefan provided the SSUSI dataset and associated tools. Christina facilitated the comparison with *S4 index*. All authors participated in discussions and refinement of the manuscript.

Competing interests. The authors declare that they have no conflict of interest.

Acknowledgements. This work was funded by the German Science Foundation (DFG project WI4417/2-1). The authors acknowledge the NOAA National Centers for Environmental Information (https://ngdc.noaa.gov/stp/satellite/poes/dataaccess.html) for the POES and Metop particle data used in this study. The Kp-index is provided from GFZ Potzdam (https://kp.gfz-potsdam.de). We thank Juan Rodriguez (NOAA) for a helpful comment on the energy range of the crosstalking particles and Frank Heymann (DLR) for fruitful discussions on the background channels. The authors would like to thank ChatGPT for linguistic assistance in refining the manuscript.

https://doi.org/10.5194/egusphere-2025-1256
Preprint. Discussion started: 28 March 2025

References

Andersson, M. E., Verronen, P. T., Rodger, C. J., Clilverd, M. A., and Wang, S.: Longitudinal hotspots in the mesospheric OH variations due to energetic electron precipitation, Atmospheric Chemistry and Physics, 14, 1095–1105, https://doi.org/10.5194/acp-14-1095-2014, 2014.

Arras, C. and Wickert, J.: Estimation of ionospheric sporadic E intensities from GPS radio occultation measurements, Journal of Atmospheric and Solar-Terrestrial Physics, 171, 60–63, https://doi.org/10.1016/j.jastp.2017.08.006, vertical Coupling in the Atmosphere-Ionosphere System: Recent Progress, 2018.

Asikainen, T. and Mursula, K.: Recalibration of NOAA/MEPED energetic proton measurements, J. Atmos. Sol. Terr. Phys., 73, 335–347, https://doi.org/10.1016/j.jastp.2009.12.011., 2011.

Asikainen, T. and Mursula, K.: Correcting the NOAA/MEPED energetic electron fluxes for detector efficiency and proton contamination, Journal of Geophysical Research: Space Physics, 118, 6500–6510, https://doi.org/10.1002/jgra.50584, 2013.

Asikainen, T., Mursula, K., and Maliniemi, V.: Correction of detector noise and recalibration of NOAA/MEPED energetic proton fluxes, J. Geophys. Res., 117, A09 204, https://doi.org/10.1029/2012JA017593, 2012.

Baker, D. N., Kanekal, S. G., Hoxie, V. C., Henderson, M. G., Li, X., Spence, H. E., Elkington, S. R., Friedel, R. H. W., Goldstein, J., Hudson, M. K., Reeves, G. D., Thorne, R. M., Kletzing, C. A., and Claudepierre, S. G.: A Long-Lived Relativistic Electron Storage Ring Embedded in Earth's Outer Van Allen Belt, Science, 340, 186–190, https://doi.org/10.1126/science.1233518, 2013.

Baker, D. N., Jaynes, A. N., Hoxie, V. C., Thorne, R. M., Foster, J. C., Li, X., Fennell, J. F., Wygant, J. R., Kanekal, S. G., Erickson, P. J., Kurth, W., Li, W., Ma, Q., Schiller, Q., Blum, L., Malaspina, D. M., Gerrard, A., and Lanzerotti, L. J.: An impenetrable barrier to ultrarelativistic electrons in the Van Allen radiation belts, Nature, 515, 531–534, https://doi.org/10.1038/nature13956, 2014.

Baker, D. N., Hoxie, V., Zhao, H., Jaynes, A. N., Kanekal, S., Li, X., and Elkington, S.: Multiyear Measurements of Radiation Belt Electrons: Acceleration, Transport, and Loss, Journal of Geophysical Research (Space Physics), 124, 2588–2602, https://doi.org/10.1029/2018JA026259, 2019.

Bartels, J., Heck, N. H., and Johnston, H. F.: The three-hour-range index measuring geomagnetic activity, Terrestrial Magnetism and Atmospheric Electricity, 44, 411–454, https://doi.org/10.1029/TE044i004p00411, 1939.

Bender, S., Espy, P. J., and Paxton, L. J.: Validation of SSUSI-derived auroral electron densities: comparisons to EISCAT data, Ann. Geophys., 39, 899–910, https://doi.org/10.5194/angeo-39-899-2021, 2021.

Crutzen, P. J., Isaksen, I. S. A., and Reid, G. C.: Solar Proton Events: Stratospheric Sources of Nitric Oxide, Science, 189, 457–459, https://doi.org/10.1126/science.189.4201.457, 1975.

Evans, D., Garrett, H., Jun, I., Evans, R., and Chow, J.: Long-term observations of the trapped high-energy proton population (L<4) by the NOAA Polar Orbiting Environmental Satellites (POES), Advances in Space Research, 41, 1261–1268, https://doi.org/10.1016/j.asr.2007.11.028, 2008.

Evans, D. S. and Greer, M. S.: Polar Orbiting Environmental Satellite Space Environment Monitor - 2, Instrument Descriptions and Archive Data Documentation, National Oceanic and Atmospheric Administration, NOAA Space Environ. Lab, Boulder, Colorado, USA, version 1.4b, including TED calibrations, 2004a.

Evans, D. S. and Greer, M. S.: Polar Orbiting Environmental Satellite Space Environment Monitor - 2, Instrument Descriptions and Archive Data Documentation, National Oceanic and Atmospheric Administration, NOAA Space Environ. Lab, Boulder, Colorado, USA, version 2.0, 2004b.

https://doi.org/10.5194/egusphere-2025-1256
Preprint. Discussion started: 28 March 2025

Evans, D. S. and Greer, M. S.: Polar Orbiting Environmental Satellite Space Environment Monitor - 2, Instrument Descriptions and Archive Data Documentation, National Oceanic and Atmospheric Administration, NOAA Space Environ. Lab, Boulder, Colorado, USA, version 2.0, 2006.

Funke, B., Baumgaertner, A., Calisto, M., Egorova, T., Jackman, C. H., Kieser, J., Krivolutsky, A., López-Puertas, M., Marsh, D. R., Reddmann, T., Rozanov, E., Salmi, S.-M., Sinnhuber, M., Stiller, G. P., Verronen, P. T., Versick, S., von Clarmann, T., Vyushkova, T. Y., Wieters, N., and Wissing, J. M.: Composition changes after the "Halloween" solar proton event: the High Energy Particle Precipitation in the Atmosphere (HEPPA) model versus MIPAS data intercomparison study, Atmospheric Chemistry and Physics, 11, 9089–9139, https://doi.org/10.5194/acp-11-9089-2011, 2011.

Gelinas, L. J. and Hecht, J. H.: Calibration/validation final report for the Special Sensor Ultraviolet Limb Imager (SSULI) and the Special Sensor Ultraviolet Spectrographic Imager (SSUSI) on the Defense Meteorological Satellite Program (DMSP) F19 Spacecraft, Aerospace Report TOR-2016-00996, Space and Missile Systems Center, Air Force Space Command, 483 N. Aviation Blvd., El Segundo, CA, USA, attn: SMC/RS, 90245-2808, 2016.

Green, J.: TED Data Processing - ALGORITHM THEORETICAL BASIS DOCUMENT - Version 1.0, Tech. rep., NOAA National Geophysical Data Center, https://ngdc.noaa.gov/stp/satellite/poes/docs/NGDC/TEDprocessingATBD_V1.doc, version 1.0, 2013.

Heath, D. F., Krueger, A. J., and Crutzen, P. J.: Solar proton event - Influence on stratospheric ozone, Science, 197, 886–889, https://doi.org/10.1126/science.197.4306.886, 1977.

Kavanagh, A. J., Cobbett, N., and Kirsch, P.: Radiation Belt Slot Region Filling Events: Sustained Energetic Precipitation Into the Mesosphere, Journal of Geophysical Research: Space Physics, 123, 7999–8020, https://doi.org/10.1029/2018JA025890, 2018.

Kim, H., Shiokawa, K., Park, J., Miyoshi, Y., Miyashita, Y., Stolle, C., Connor, H. K., Hwang, J., Buchert, S., Kwon, H.-J., Nakamura, S., Nakamura, K., Oyama, S.-I., Otsuka, Y., Nagatsuma, T., and Sakaguchi, K.: Isolated Proton Aurora Driven by EMIC Pc1 Wave: PWING, Swarm, and NOAA POES Multi-Instrument Observations, Geophysical Research Letters, 48, e2021GL095 090, https://doi.org/10.1029/2021GL095090, e2021GL095090 2021GL095090, 2021.

Knight, H. K.: Auroral ionospheric E region parameters obtained from satellite-based far-ultraviolet and ground-based ionosonde observations – effects of proton precipitation, Annales Geophysicae, 39, 105–118, https://doi.org/10.5194/angeo-39-105-2021, 2021.

Knight, H. K., Strickland, D. J., Correira, J., Hecht, J. H., and Straus, P. R.: An empirical determination of proton auroral far ultraviolet emission efficiencies using a new nonclimatological proton flux extrapolation method, Journal of Geophysical Research: Space Physics, 117, https://doi.org/https://doi.org/10.1029/2012JA017672, 2012.

Knight, H. K., Galkin, I. A., Reinisch, B. W., and Zhang, Y.: Auroral Ionospheric E Region Parameters Obtained From Satellite-Based Far Ultraviolet and Ground-Based Ionosonde Observations: Data, Methods, and Comparisons, J. Geophys. Res. Space Phys., 123, 6065–6089, https://doi.org/10.1029/2017ja024822, 2018.

Lam, M. M., Horne, R. B., Meredith, N. P., Glauert, S. A., Moffat-Griffin, T., and Green, J. C.: Origin of energetic electron precipitation >30 keV into the atmosphere, Journal of Geophysical Research: Space Physics, 115, https://doi.org/10.1029/2009JA014619, 2010.

Laundal, K. M. and Richmond, A. D.: Magnetic Coordinate Systems, Space Sci. Rev., 206, 27–59, https://doi.org/10.1007/s11214-016-0275-y, 2017.

Li, X., Baker, D. N., Kanekal, S. G., Looper, M., and Temerin, M.: Long term measurements of radiation belts by SAMPEX and their variations, Geophysical Research Letters, 28, 3827–3830, https://doi.org/10.1029/2001GL013586, 2001.

McPeters, R. D. and Jackman, C. H.: The response of ozone to solar proton events during solar cycle 21: The observations, Journal of Geophysical Research: Atmospheres, 90, 7945–7954, https://doi.org/10.1029/JD090iD05p07945, 1985.

https://doi.org/10.5194/egusphere-2025-1256
Preprint. Discussion started: 28 March 2025

Nesse Tyssøy, H., Sandanger, M. I., Ødegaard, L.-K. G., Stadsnes, J., Aasnes, A., and Zawedde, A. E.: Energetic electron precipitation into the middle atmosphere-Constructing the loss cone fluxes from MEPED POES, Journal of Geophysical Research: Space Physics, 121, 5693–5707, https://doi.org/10.1002/2016JA022752, 2016.

Ødegaard, L.-K. G., Tyssøy, H. N., Sandanger, M. I. J., Stadsnes, J., and Søraas, F.: Space Weather impact on the degradation of NOAA POES MEPED proton detectors, J. Space Weather Space Clim., 6, A26, https://doi.org/10.1051/swsc/2016020, 2016.

Paxton, L. J., Meng, C.-I., Fountain, G. H., Ogorzalek, B. S., Darlington, E. H., Gary, S. A., Goldsten, J. O., Kusnierkiewicz, D. Y., Lee, S. C., Linstrom, L. A., Maynard, J. J., Peacock, K., Persons, D. F., and Smith, B. E.: Special sensor ultraviolet spectrographic imager: an instrument description, in: Instrumentation for Planetary and Terrestrial Atmospheric Remote Sensing, edited by Chakrabarti, S. and Christensen, A. B., SPIE, https://doi.org/10.1117/12.60595, 1992.

Paxton, L. J., Schaefer, R. K., Zhang, Y., and Kil, H.: Far ultraviolet instrument technology, J. Geophys. Res. Space Phys., 122, 2706–2733, https://doi.org/10.1002/2016ja023578, 2017.

Paxton, L. J., Schaefer, R. K., Zhang, Y., Kil, H., and Hicks, J. E.: SSUSI and SSUSI-Lite: Providing Space Situational Awareness and Support for Over 25 Years, Johns Hopkins APL Tech. Dig., 34, 388–400, 2018.

Peck, E. D., Randall, C. E., Green, J. C., Rodriguez, J. V., and Rodger, C. J.: POES MEPED differential flux retrievals and electron channel contamination correction, Journal of Geophysical Research: Space Physics, 120, 4596–4612, https://doi.org/10.1002/2014JA020817, 2015.

Richmond, A. D.: Ionospheric Electrodynamics Using Magnetic Apex Coordinates., Journal of Geomagnetism and Geoelectricity, 47, 191–212, https://doi.org/10.5636/jgg.47.191, 1995.

Ross, J. P. J., Glauert, S. A., Horne, R. B., Watt, C. E. J., and Meredith, N. P.: On the Variability of EMIC Waves and the Consequences for the Relativistic Electron Radiation Belt Population, Journal of Geophysical Research: Space Physics, 126, e2021JA029 754, https://doi.org/10.1029/2021JA029754, e2021JA029754 2021JA029754, 2021.

Rusch, D., Gérard, J.-C., Solomon, S., Crutzen, P., and Reid, G.: The effect of particle precipitation events on the neutral and ion chemistry of the middle atmosphere—I. Odd nitrogen, Planetary and Space Science, 29, 767–774, https://doi.org/10.1016/0032-0633(81)90048-9, 1981.

Sandanger, M. I., Ødegaard, L.-K. G., Nesse Tyssøy, H., Stadsnes, J., Søraas, F., Oksavik, K., and Aarsnes, K.: In-flight calibration of NOAA POES proton detectors—Derivation of the MEPED correction factors, Journal of Geophysical Research: Space Physics, 120, 9578–9593, https://doi.org/10.1002/2015JA021388, 2015.

Selesnick, R. S., Baker, D. N., Jaynes, A. N., Li, X., Kanekal, S. G., Hudson, M. K., and Kress, B. T.: Observations of the inner radiation belt: CRAND and trapped solar protons, Journal of Geophysical Research (Space Physics), 119, 6541–6552, https://doi.org/10.1002/2014JA020188, 2014.

Selesnick, R. S., Tu, W., Yando, K., Millan, R. M., and Redmon, R. J.: POES/MEPED Angular Response Functions and the Precipitating Radiation Belt Electron Flux, Journal of Geophysical Research: Space Physics, 125, e2020JA028 240, https://doi.org/10.1029/2020JA028240, e2020JA028240 10.1029/2020JA028240, 2020.

Solomon, S., Rusch, D., Gérard, J., Reid, G., and Crutzen, P.: The effect of particle precipitation events on the neutral and ion chemistry of the middle atmosphere: II. Odd hydrogen, Planetary and Space Science, 29, 885–893, https://doi.org/10.1016/0032-0633(81)90078-7, 1981.

https://doi.org/10.5194/egusphere-2025-1256
Preprint. Discussion started: 28 March 2025

Solomon, S., Reid, G. C., Rusch, D. W., and Thomas, R. J.: Mesospheric ozone depletion during the Solar Proton Event of July 13, 1982 Part II. Comparison between theory and measurements, Geophysical Research Letters, 10, 257–260, https://doi.org/10.1029/GL010i004p00257, 1983.

Søraas, F., Sandanger, M. I., and Smith-Johnsen, C.: NOAA POES and MetOp particle observations during the 17 March 2013 storm, Journal of Atmospheric and Solar-Terrestrial Physics, 177, 115–124, https://doi.org/10.1016/j.jastp.2017.09.004, dynamics of the Sun-Earth System: Recent Observations and Predictions, 2018.

SSUSI: Data products, available at: https://ssusi.jhuapl.edu/data_products, last access: 21 September, 2020.

Strickland, D. J., Jasperse, J. R., and Whalen, J. A.: Dependence of auroral FUV emissions on the incident electron spectrum and neutral atmosphere, J. Geophys. Res. Space Phys., 88, 8051, https://doi.org/10.1029/ja088ia10p08051, 1983.

Turner, D. L., Shprits, Y., Hartinger, M., and Angelopoulos, V.: Explaining sudden losses of outer radiation belt electrons during geomagnetic storms, Nature Physics, 8, 208–212, https://doi.org/10.1038/nphys2185, 2012.

van Allen, J. A.: The Geomagnetically Trapped Corpuscular Radiation, Journal of Geophysical Research, 64, 1683–1689, https://doi.org/10.1029/JZ064i011p01683, 1959.

van Allen, J. A.: Origins of magnetospheric physics., University of Iowa Press, 1983.

Van Zandt, T., Clark, W., and Warnock, J.: Magnetic apex coordinates: A magnetic coordinate system for the ionospheric F2 layer, vol. 55, Environmental Research Laboratories, 1972.

Wissing, J. M. and Kallenrode, M.-B.: Atmospheric Ionization Module Osnabrück (AIMOS): A 3-D model to determine atmospheric ionization by energetic charged particles from different populations, Journal of Geophysical Research: Space Physics, 114, https://doi.org/10.1029/2008JA013884, 2009.

Wu, D. L.: Ionospheric S4 Scintillations from GNSS Radio Occultation (RO) at Slant Path, Remote Sensing, 12, https://doi.org/10.3390/rs12152373, 2020.

Yakovchuk, O. and Wissing, J.: Magnetic local time asymmetries in precipitating electron and proton populations with and without substorm activity, Annales Geophysicae, 37, 1063–1077, https://doi.org/10.5194/angeo-37-1063-2019, 2019.

Yando, K., Millan, R. M., Green, J. C., and Evans, D. S.: A Monte Carlo simulation of the NOAA POES Medium Energy Proton and Electron Detector instrument, Journal of Geophysical Research: Space Physics, 116, https://doi.org/10.1029/2011JA016671, 2011.